Galactic rotation curves of low surface brightness galaxies using core-halo fuzzy dark matter configurations

Iván Álvarez-Rios[1,*] Tula Bernal,[2,†] Pierre-Henri Chavanis[3,‡] and Francisco S. Guzmán[1,§]

[1]*Instituto de Física y Matemáticas, Universidad Michoacana de San Nicolás de Hidalgo, Edificio C-3, Cd. Universitaria, 58040 Morelia, Michoacán, México*
[2]*Área de Física, Depto. de Preparatoria Agrícola, Universidad Autónoma Chapingo, Km 38.5 Carretera México-Texcoco, Texcoco 56230, Edo. Méx., México*
[3]*Laboratoire de Physique Théorique, Université Paul Sabatier, 118 route de Narbonne 31062 Toulouse, France*

In this work, we construct galactic halos in order to fit the rotation curves (RCs) of a sample of low surface brightness (LSB) galaxies. These halos are made of fuzzy dark matter (FDM) with a multimode expansion of nonspherical modes that in average contribute to the appropriate density profile consisting of a core and an envelope needed to fit the rotation curves. The coefficients of the expansion are calculated using a genetic algorithm, that minimizes the difference between the spatial average density of the multimode order parameter describing the FDM and the target dark matter density that fits the RCs. The FDM halos are constructed assuming a solitonic core at the center and two types of envelopes, Navarro-Frenk-White and pseudoisothermal density profiles. The resulting FDM configurations are then evolved in order to show how the average density changes in time due to the secular dynamical evolution, along with a condensation process that lead to the growth of the solitonic core.

I. INTRODUCTION

Fuzzy dark matter (FDM) is a dark matter candidate, consisting of an ultralight spin zero boson that has received recent attention because it apparently solves some of the traditional problems of cold dark matter (CDM), namely the cusp-core and the too-big-to-fail problems as explained in recent reviews [1–5]. The reason is that the formation of very small scale structures is prevented by the uncertainty principle for such an ultralight particle and the mass power spectrum is cut off at small scales. In addition, the tiny mass of the boson implies smooth galactic cores as opposed to the cuspy shape obtained from predictions of CDM.

At cosmic scales the model has been deeply studied in structure formation simulations (SFS) (see, e.g., [6–11]), that are promising and already involve the dynamics of baryonic matter. At local scales the works concentrate on the formation of core-tail halos like those obtained in SFS, for example through the merger of multiple cores (see, e.g., [7,12,13]) that end up with the core surrounded by a typical granular structure that in average shows a Navarro-Frenk-White (NFW) density profile [14]. Construction of

target density profiles is also a subject of current interest, because the wave function describing the FDM at local scales suggests a clear multimode dependency. This approach has been developed for SFS [15] as well at local scales with the construction of on demand multimode density profiles whose stability is studied with simulations [16,17].

Now, the boson mass m_B in the FDM, in order to address the small scale problems (core density profile and suppression of the small-scale structure) and to behave like CDM on large scales, must be of the order of $m_B \sim 10^{-23}$–10^{-21} eV. From the high-redshift luminosity function of galaxies we have the constraint for the boson mass $m_B > 1.2 \times 10^{-22}$ eV [18], while Iršič *et al.* [19], Armengaud *et al.* [20] derive a stringent constraint, indicating $m_B \gtrsim 2 \times 10^{-21}$ eV. On the lower limit of the boson mass, the most used value is $m_B \sim 10^{-22}$ eV in order to solve the small-scale problems of CDM. In the cosmological context, the analysis of cosmic microwave background (CMB) and galaxy clustering data in, e.g., Hlozek *et al.* [21], establishes a constraint for the boson mass in the FDM model of $m_B > 10^{-24}$ eV. Considering the galaxy UV-luminosity function and reionization constraints, Bozek *et al.* [22] determined a minimum mass requirement of $m_B > 10^{-23}$ eV. Also, from Lyman-α observations, the constraint is $m_B > 10^{-23}$ eV [23]. This value is in tension with the results by Rindler-Daller and Shapiro [24], setting the minimum value for

---
*Contact author: ivan.alvarez@umich.mx
†Contact author: tbernalm@chapingo.mx
‡Contact author: chavanis@irsamc.ups-tlse.fr
§Contact author: francisco.s.guzman@umich.mx

063502-1

$m_B > 10^{-25}$ eV. This indicates there is no consensus on the accurate mass of the ultralight boson and that further exploration is still necessary. Meanwhile we explore the viability of the model at local scales. Notice that self-interaction is another parameter that influences the construction and phenomenology of structures within the bosonic dark matter model, and that it could substantially change the constraints on the boson mass [see e.g. [25–33]].

In this work, likewise in [17], we focus on the construction of multimode FDM configurations, in particular with solitonic core and an envelope with NFW and pseudoisothermal (PISO) density profiles that fit rotation curves of low surface brightness (LSB) galaxies, and study their evolution in order to study their behavior and stability properties.

The article is organized as follows. In Sec. II we describe the method we use to construct multimode halos, in Sec. III we study the evolution of these configurations, and finally in Sec. IV we draw some conclusions.

II. CONSTRUCTION OF GALACTIC CORE-HALO PROFILES

A. Basic assumptions

The dynamics of FDM is modeled with the Schrödinger-Poisson (SP) system:

$$i\hbar \frac{\partial \Psi}{\partial t} = -\frac{\hbar^2}{2m_B}\nabla^2\Psi + m_B V\Psi, \qquad (1)$$

$$\nabla^2 V = 4\pi G(\rho - \bar{\rho}), \qquad (2)$$

where Ψ is an order parameter related to the matter density through $\rho := m_B|\Psi|^2$, with m_B the boson particle mass, $\hbar$ the reduced Planck constant, G the gravitational constant, and $\bar{\rho} = \frac{1}{|D|}\int_D \rho d^3x$ the spatially averaged density calculated within a spatial domain D with volume $|D| := \int_D d^3x$, where the construction of configurations is implemented and where the evolution is carried out. The gravitational potential V is sourced by the difference between the density and its spatial average.

We want to construct solutions of the Schrödinger-Poisson (SP) system that are consistent with some galactic rotation curves. In order to construct the wave function of the core-halo, we follow a similar strategy as that designed in [15,16]. We assume there is a target density profile ρ_T, and the goal is to construct a corresponding wave function Ψ_0 that is consistent with this density profile and satisfies the SP system. For this, we consider the target density to be a spherically symmetric function, depending on the radial coordinate r only. This makes possible to solve Poisson equation (2) in spherical symmetry which can be written as the following first order system:

$$\frac{dV_T}{dr} = G\frac{M_T}{r^2}, \qquad (3)$$

$$\frac{dM_T}{dr} = 4\pi r^2 \rho_T, \qquad (4)$$

where ρ_T is the target density and M_T is the radial mass function. Once Poisson equation is solved, the resulting potential V_T is a function of r. This potential is injected into the stationary version of the Gross-Pitaevskii equation (1). This equation is reminiscent of the problem of the hydrogen atom, with the notable difference being the replacement of the Coulomb potential by the potential V_T, which is written as a Sturm-Liouville problem

$$-\frac{\hbar^2}{2m_B}\frac{1}{r^2}\frac{\partial}{\partial r}\left(r^2\frac{\partial\psi_j}{\partial r}\right) + \frac{\hbar^2}{2m_B}\frac{L^2}{r^2}\psi_j + m_B V_T\psi_j = E_j\psi_j, \quad (5)$$

where

$$L^2 = -\left[\frac{1}{\sin\theta}\frac{\partial}{\partial\theta}\left(\sin\theta\frac{\partial}{\partial\theta}\right) + \frac{1}{\sin^2\theta}\frac{\partial^2}{\partial\phi^2}\right] \qquad (6)$$

is the squared angular momentum operator and j labels the eigenstate ψ_j with eigenenergy E_j. To solve this equation, we assume a separation of variables for $\psi_j :=$ $\psi_{n\ell m}(r,\theta,\phi) = R_{n\ell}(r)Y_l^m(\theta,\phi)$, where $Y_l^m(\theta,\phi)$ are the spherical harmonics and $R_{n\ell}$ is expressed as $R_{n\ell} := u_{n\ell}/r$, with $u_{n\ell}$ satisfying the following radial equation:

$$-\frac{\hbar^2}{2m_B}\frac{d^2u_{n\ell}}{dr^2} + \left(\frac{\hbar^2}{2m_B}\frac{\ell(\ell+1)}{r^2} + m_B V_T(r)\right)u_{n\ell} = E_{nl}u_{nl}, \qquad (7)$$

where n, ℓ, and m are "quantum numbers," and where we have used the identity $L^2 Y_{lm} = l(l+1)Y_{lm}$. We name the wave function Ψ_0 as the one that fits the target density, which we express as a linear combination of the eigenfunctions ψ_j

$$\Psi_0 = \sum_j a_j\psi_j e^{-iE_j t/\hbar}. \qquad (8)$$

The density profile $|\Psi_0|^2$ associated with the wave function is given by

$$|\Psi_0|^2 = \left(\sum_j a_j\psi_j e^{-iE_j t/\hbar}\right)\left(\sum_k a_k^*\psi_k^* e^{iE_k t/\hbar}\right)$$
$$= \sum_j |a_j|^2|\psi_j|^2 + \sum_{j\neq k} a_j a_k^*\psi_j\psi_k^* e^{i(E_k-E_j)t/\hbar}. \qquad (9)$$

An essential assumption when fitting structure densities in structure formation simulations or multicore collisions, is that ρ_T is a time-averaged quantity, as well as a spatially

averaged quantity along various radial directions. Therefore, we assume that the target density can be decomposed as follows:

$$\langle|\Psi_0|^2\rangle_{T\to\infty} := \lim_{T\to\infty}\frac{1}{T}\int_0^T|\Psi_0(t,\vec{x})|^2dt$$
$$= \frac{1}{4\pi}\sum_{n,\ell}(2\ell+1)|\tilde{a}_{n\ell}|^2|R_{n\ell}|^2, \quad (10)$$

where T is the time-window used to calculate *time-averages*. To derive Eq. (10) we have used the identity $\sum_m |Y_{lm}(\theta,\phi)|^2 = (2l+1)/4\pi$. In this formula, the coefficients are written as $a_{n\ell m} = \tilde{a}_{n\ell}e^{i\Theta_{n\ell m}}$, where $\Theta_{n\ell m}$ are random phases with values between 0 and 2π. Another alternative is to consider a *spatial-average* over the solid angle $\Omega := [0,\pi]\times[0,2\pi]$ as follows:

$$\langle|\Psi_0|^2\rangle_\Omega := \frac{1}{4\pi}\int_\Omega|\Psi_0(t,\vec{x})|^2d\Omega$$
$$= \frac{1}{4\pi}\sum_{n,\ell}(2\ell+1)|\tilde{a}_{n\ell}|^2|R_{n\ell}|^2. \quad (11)$$

In this way, temporal and spatial averages are assumed equal and the target density must satisfy $\rho_T \approx m_B\langle|\Psi_0|^2\rangle_{T\to\infty} = m_B\langle|\Psi_0|^2\rangle_\Omega$. Then, we can simply write $\rho_T \approx m_B\langle|\Psi_0|^2\rangle$ referring to either angular or time average. However, it must also hold that $V_T \approx \langle V\rangle$.

An important aspect of Ψ_0 is whether it corresponds to a virialized configuration or not. In order to answer this question, we calculate the quantity $Q_0 = 2K_0 + W_0$, where

$$K_0 = \frac{\hbar^2}{2m_B}\int|\nabla\Psi_0|^2d^3x = -\frac{\hbar^2}{2m_B}\int_D\Psi_0^*\nabla^2\Psi_0 d^3x, \quad (12)$$

is the kinetic energy and

$$W_0 = \frac{m_B}{2}\int_D V_T|\Psi_0|^2d^3x \quad (13)$$

is the gravitational energy. In an ideally virialized configuration $Q_0 = 0$. This quantity can be written in terms of a spectral decomposition as

$$Q_0 = \sum_{n,l}(2\ell+1)|\tilde{a}_{n\ell}|^2Q_{n\ell}, \quad (14)$$

with $Q_{n\ell} = 2K_{n\ell} + W_{n\ell}$, where $K_{n\ell}$ and $W_{n\ell}$ are the matrix elements of the kinetic and potential energies with respect to the supposed basis of the eigenproblem given by

$$K_{n\ell} = -\frac{\hbar^2}{2m_B}\int R_{n\ell}\left[\frac{d}{dr}\left(r^2\frac{dR_{n\ell}}{dr}\right) - \ell(\ell+1)R_{n\ell}\right]dr, \quad (15)$$

and

$$W_{n\ell} = \frac{m_B}{2}\int V_TR_{n\ell}^2r^2dr. \quad (16)$$

On the other hand, from Eqs. (7), (15), and (16) we obtain the identity $K_0 + 2W_0 = E_0$ with

$$E_0 = \frac{1}{m}\int\sum_{nl}R_{nl}(r)^2(2l+1)|\tilde{a}_{nl}|^2E_{nl}r^2dr, \quad (17)$$

where $E_{n\ell}$ are the eigenvalues (notice that E_0 is an eigenvalue and not the total energy that could be confused with $K_0 + W_0$). Therefore, we have $Q_0 = 2E_0 - 3W_0$ (in components form $K_{n\ell} + 2W_{n\ell} = E_{n\ell}$ and $Q_{n\ell} = 2E_{n\ell} - 3W_{n\ell}$). The mass reads

$$M_0 = \int\rho d^3x = m_B\int|\Psi_0|^2d^3x, \quad (18)$$

hence

$$M_0 = \int\sum_{nl}R_{nl}(r)^2(2l+1)|\tilde{a}_{nl}|^2r^2dr. \quad (19)$$

We numerically verify that, in general, the individual terms $Q_{n\ell}$ are different from zero and can have different sign for different values of n and ℓ. That is, each mode of superposition is not virialized, however we find a superposition such that $Q_0 \approx 0$.

The construction of Ψ_0 reduces to the calculation of the coefficients $\tilde{a}_{n\ell}$ of the expansion for the target density in equation (10) or equivalently (11) and a specific way in which the constraint $Q_0 \approx 0$ is satisfied. Once these coefficients are determined, it becomes possible to reconstruct a wave function that is consistent with the stationary SP system and at the same time has an average density consistent with a core-halo target density.

The steps to construct the FDM core-halo configuration are summarized as follows:

(1) Start with a given target density ρ_T. In order to have a finite integrated mass we follow the recipe in [16] that suggests to modulate the target density with a Gaussian $e^{-r^2/(2r_0^2)}$, having r_0 as the value for which $\frac{\rho_T(0)}{\rho_T(r_0)} \sim 10^3$.

(2) Solve Poisson equation (3)–(4) for such density in the domain $r \in [0, 2r_0]$, as also suggested in [16].

(3) Use the resulting gravitational potential V_T to solve Eq. (7) for all combinations of n and ℓ to be considered.

(4) Then find the coefficients a_j that minimize an error function between $\rho := m_B\langle|\Psi|^2\rangle$ and ρ_T.

In the following subsection, we elaborate on the ingredients of step 4.

B. Description of the fitting method

The expansion of the wave function (8) can have a large number of terms, and they have to be such that $\rho - \rho_T$, or a norm of it, is minimum. Notice that this problem is reduced to locating the minimum of a function (a given norm of the error) that depends on a large number of parameters [the coefficients of expansion (8)]. The use of a genetic algorithm (GA) for the solution of this type of problems is an option, on the one hand because the concept of DNA can use a large number of genes that we identify with the coefficients of the expansion, and on the other hand the mutation of DNA allows the possibility to exit from local minima.

A GA is inspired by the theory of evolution, which assumes the existence of a population of individuals characterized by their DNA composed of a chain of genes, which determine their fitness for survival in an environment. The best-adapted individuals, whose adaptation is measured in terms of a fitness function, have a greater chance of surviving and consequently a greater chance of reproducing, passing their genes on to their offspring in a new generation. Offspring results from a combination of their parents' genes, while a speed up in evolution is due to mutation. This process over many generations leads to a population much better adapted than the initial one.

We adapt this method to solve our minimization problem as follows. We start with a population of individuals, each one with random coefficients in the expansion (8), that may evolve toward a population of individuals that approach the condition that a norm of $\rho - \rho_T$ is small. For this purpose we define a population of individuals, each one with genes given by the sequence of coefficients a_j of the expansion (8) and DNA given by the set of coefficients $\tilde{a}_{n\ell}$. The maximum number of genes considered is $N_{\text{DNA}} = n_{\max}\ell_{\max}$, where the quantum numbers take on the values $n = 1, 2, \ldots, n_{\max}$ and $\ell = 0, 1, \ldots, \ell_{\max} - 1$. We define the fitness of an individual as a decreasing function of the difference between ρ and ρ_T, which is bigger for better-adapted individuals and is near a virialized state such that $Q_0 \approx 0$. We thus define the fitness function as

$$\eta = \frac{1}{1 + |Q_0|}\left[\frac{1}{r_{\max}}\int_0^{r_{\max}}\frac{(\rho_T - \rho)^2}{\rho_T}\,dr\right]^{-1}, \quad (20)$$

where the term $1 + |Q_0|$ is not significant when $|Q_0| < 1$, but when $|Q_0| > 1$, the value of the fitness function decreases for profiles far from a virialized state. Finally, $r_{\max} = 2r_0$ is the upper boundary of the numerical domain where the eigenvalue problem (5) is solved.

The operation of the GA is based on the random generation of an initial population of N_{org} organisms. We calculate the fitness function η of all individuals, and choose the k most fitted organism. Following an elitist approach, these selected individuals prevail through the next generation. From these k organisms, N_{cross} are randomly chosen to cross-over and produce children for the next generation; in a biological context, one would typically choose $N_{\text{cross}} = 2$, but this is not a limitation in a GA and $N_{\text{cross}} = 5$ worked better. These selected parents will randomly share their genetic material, namely the coefficients of the expansion, to create a new individual. This process is repeated $N_{\text{org}} - k$ times until the initial population size N_{org} is completed again.

The organisms in the new generation can potentially adapt more effectively with a mutation process that works as follows. We generate a new random number $\beta_{n\ell}$ ranging from 0 to 1, representing the likelihood that the gene $\tilde{a}_{n\ell}$ undergoes a mutation. Each gene has its own probability of change. Subsequently, a new random number $\gamma_{n\ell}$ is generated, and the mutation occurs if $\gamma_{n\ell}$ exceeds $\beta_{n\ell}$. In such cases, the coefficient $\tilde{a}_{n\ell}$ is altered to $\alpha\tilde{a}_{n\ell}$, where α is a randomly selected number within the range of -1.5 to 1.5 for all values of n and ℓ.

Finally, a second type of mutation, known as differential mutation is applied. This mutation involves selecting the ith organism with DNA defined by the coefficients $\tilde{a}_{n\ell}^{(i)}$ along with a fitness $\eta^{(i)}$. Subsequently, two other organisms with DNA $\tilde{a}_{n\ell}^{(1)}$ and $\tilde{a}_{n\ell}^{(2)}$ are randomly selected. A new organism is then created by linearly combining these coefficients as $\tilde{a}_{n\ell}^{(\text{new},i)} = \tilde{a}_{n\ell}^{(i)} + \delta(\tilde{a}_{n\ell}^{(1)} - \tilde{a}_{n\ell}^{(2)})$, where δ is a number between 0 and 1, with fitness $\eta^{(\text{new},i)}$. If it happens that $\eta^{(\text{new},i)} > \eta^{(i)}$, the ith organism is replaced by the new organism. This process is repeated for $i = 1, 2, \ldots, N_{\text{org}}$.

Notice that the fitness function is a norm of the error between the density of the multipolar expansion and the target density. Considering the randomness in various stages of the GA it could well happen that different sets of coefficients of the expansion, or equivalently individuals with different DNA, may have similar values of η. In this sense, the expansion of the profile can be degenerate.

Now, our goal is to tune the galactic dark matter densities. Inspired by [15,16] we use a certain type of target density profile which we discuss below.

C. Models for target density

Core-NFW model. Simulations of binary systems, multi-core mergers, and more complex scenarios like structure formation simulations reveal that the time-spatial averages of the formed structures exhibit a spherical profile with a soliton core at the center. This core, with density similar to that of the ground state of the SP system (see, e.g., Guzmán and Ureña López [34]), is modeled with the empirical profile [6,12]:

$$\rho_{\text{core}}(r) = \rho_c\left[1 + 0.091\left(\frac{r}{r_c}\right)^2\right]^{-8}, \quad (21)$$

where we can find the relation between the central density ρ_c and the core radius r_c from the numerical solution of the

ground state using the boundary condition $\psi(r = 0) = 1$ in units where $\hbar = m_B = 4\pi G = 1$. If we fix $\rho_c = 1$, we can find that $r_c \approx 1.30569 \pm 0.000113$. Using the λ-scaling relation of the SP system [34], it is found that $\rho_c \approx (1.30569/r_c)^4$ for an arbitrary value of the core radius r_c. With this, we can translate the central density to physical units as

$$
\begin{aligned}
\rho_c &= \frac{\hbar^2}{4\pi G m_B^2}\left(\frac{1.30569}{r_c}\right)^4 \\
&\approx 1.983 \times 10^7 \left(\frac{\text{kpc}^4}{m_{22}^2 r_c^4}\right) M_\odot,
\end{aligned}
\tag{22}
$$

where m_{22} is defined as $m_{22} = m_B \times 10^{-22}$ eV^{-1}, and the units for r_c are $[r_c] = $ kpc.

Outside of this core, there is an envelope region that can be approximated by the NFW profile [6]:

$$
\rho_{\text{NFW}}(r) = \frac{\rho_s}{\frac{r}{r_s}\left(1 + \frac{r}{r_s}\right)^2},
\tag{23}
$$

where ρ_s and r_s are halo parameters. The complete profile of the structure takes the form [35]:

$$
\rho_{CN}(r) = \rho_{\text{sol}}(r)\Theta(r - r_t) + \rho_{\text{NFW}}(r)\Theta(r_t - r).
\tag{24}
$$

In this equation, we assume continuity, which fixes one of the two halo parameters with the relation $\rho_s = \rho_{\text{sol}}(r_t)\frac{r_t}{r_s}\left(1 + \frac{r_t}{r_s}\right)^2$.

Core-PISO model. It is well-known that a soliton nucleus forms within the halo in the FDM model since the ground state is an attractor of the SP system. However, in the envelope region, it is possible to discuss what may be the best approximation for the average profile of the envelope. One of the alternative proposals to the NFW model is the pseudoisothermal profile, which is written as

$$
\rho_{\text{PISO}}(r) = \frac{\rho_p}{1 + \left(\frac{r}{r_p}\right)^2},
\tag{25}
$$

in this case, ρ_p and r_p are halo parameters. The complete profile of the structure takes the form

$$
\rho_{CP}(r) = \rho_{\text{sol}}(r)\Theta(r - r_t) + \rho_{\text{PISO}}(r)\Theta(r_t - r),
\tag{26}
$$

similar to the core-NFW model, in which we assume continuity in the density. In this case the envelope parameters can be related as

$$
\rho_p = \rho_{\text{sol}}(r_t)\left[1 + \left(\frac{r_t}{r_p}\right)^2\right].
\tag{27}
$$

which reduces the number of fitting parameters.

D. Fitting of LSB galaxies

LSB galaxies are dominated by dark matter, thus we assume that we can fit their rotation curves with the core-NFW or core-PISO profiles. The independent parameters of a core-NFW profile are r_c, r_t, and r_s, and for the core-PISO profile, they are r_c, r_t, and r_p. We use the same strategy presented in Bernal *et al.* [36] to obtain the appropriate values for observational data in [37,38]. We additionally find the radius r_0 of the resulting configurations. Table I provides the best-fit free parameters for these galaxies.

Now, according to [39–41], the halo surface density is nearly constant and independent of the galaxy luminosity, with value $\Sigma_0 = \rho_0 r_0 = 140^{+80}_{-30} M_\odot \text{pc}^{-2}$, where ρ_0 and r_0 the halo central density and core radius [41]. We include in Table I the corresponding surface densities for both the core-NFW and core-PISO profiles, as defined in Chavanis [42], for the soliton FDM configurations: $\Sigma_0 = \rho(r_t)r_h$, with r_h the radius where the density is $\rho(r_h) = \rho(r_t)/4$, for r_t the transition radius outside the soliton region. As discussed in Appendix L of [42], the constant Σ_0 observational value is not consistent with the soliton, it decreases like $1/r^3$ as the size of the soliton increases. This suggests (see Sec. VII of [42]) to define Σ_0 with the density at the interface between the soliton and the NFW envelope, at the transition radius r_t.

As seen in Table I, from the small sample we are studying, the results do not coincide with the observational value, except for ESO4880049 with the core-PISO profile. For the core-PISO profile, the results are closer to the value obtained in [41]. The discrepancy may arise from the density profile assumed to model their huge sample of galaxies, a Burkert profile. In our case, the core-PISO profile decays slowly and is closer to the Burkert profile. We would need to simulate a large sample of galaxies with a profile closer to Burkert's to conclude if our results are in agreement with a universal surface density of dark matter.

TABLE I. Best-fit parameters for three LSB galaxies using the core-NFW and core-PISO density profiles, obtained by fixing the boson mass $m_B = 10^{-23}$ eV.

	Core-NFW				
Galaxy	r_c (kpc)	r_t (kpc)	r_s (kpc)	r_0 (kpc)	Σ_0 ($M_\odot$ pc^{-2})
ESO4880049	2.157	1.102	15.25	52.77	243
UGC11616	1.860	1.676	7.434	38.04	386
F730V1	1.867	1.841	8.118	40.01	370

	Core-PISO				
Galaxy	r_c (kpc)	r_t (kpc)	r_p (kpc)	r_0 (kpc)	Σ_0 ($M_\odot$ pc^{-2})
ESO4880049	2.269	3.260	2.631	66.49	155
UGC11616	1.850	2.474	1.792	52.82	294
F730V1	1.869	2.082	1.625	54.41	345

As described earlier, there is no consensus on the correct mass of the boson, and in our study we use a boson mass $m_B = 10^{-23}$ eV because it is near the upper bound, and allows the profiles to be adjusted for the LSB galaxies in our analysis. This mass value is on the boundary with the cosmological constraints found in [22] from the galaxy UV-luminosity function and reionization observations, and in [23] from Lyman-α observations, $m_B > 10^{-23}$ eV. It also falls within the constraints provided by [21], from CMB and galaxy clustering data, $m_B > 10^{-24}$ eV.

Now, concerning the fitting method, the parameters parameters of the GA are a population of $N_{\text{org}} = 200$ organisms, each having $n_{\max} = l_{\max} = 41$. This implies that the DNA of each organism consists of $N_{\text{DNA}} = 1681$ genes, resulting in a total of approximately 10^5 coefficients a_{nlm}, a similar number as in [16]. During reproduction, $N_{\text{cross}} = 5$ organisms contribute to creating a new organism, selected from a pool of $k = 100$ parents. Additionally, for the differential mutation, we set $\delta = 0.1$. These parameters have proven effective in identifying organisms with a fitness $\eta \approx 10^5$, or equivalently, a proportional χ^2 error $1/\eta \approx 10^{-5}$

within the initial 1000 generations, and in general a virialization factor in the range $|Q_0| < 10^{-5}$ in code units.

Using these parameters, we determined the suitable coefficients for each of the considered galaxies in Table I. The results appear in Fig. 1, which illustrate how the GA is able to construct multimode configurations that approximate the target density within the region $r < r_0$. Beyond this radius, the adjustment becomes more challenging, as seen after the a vertical red dotted line.

III. EVOLUTION OF THE GALACTIC PROFILES

We investigate the evolution of the core-halo profiles described in the previous section by evolving the wave function with the fully time-dependent SP system (1)–(2), for which we use the code CAFE [43,44]. In order to prevent the wave function from decaying into an isolated solitonic profile as suggested in Guzmán and Ureña López [45] and Bernal and Guzmán [46], and later confirmed with CAFE in [44], we implemented periodic boundary conditions that
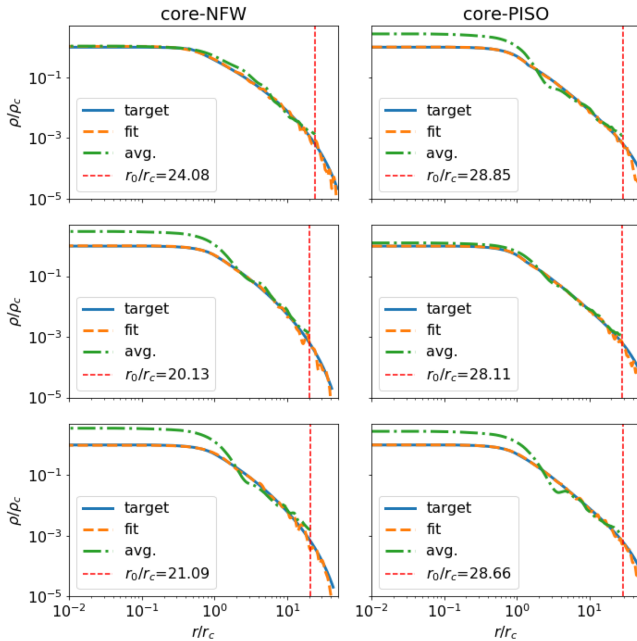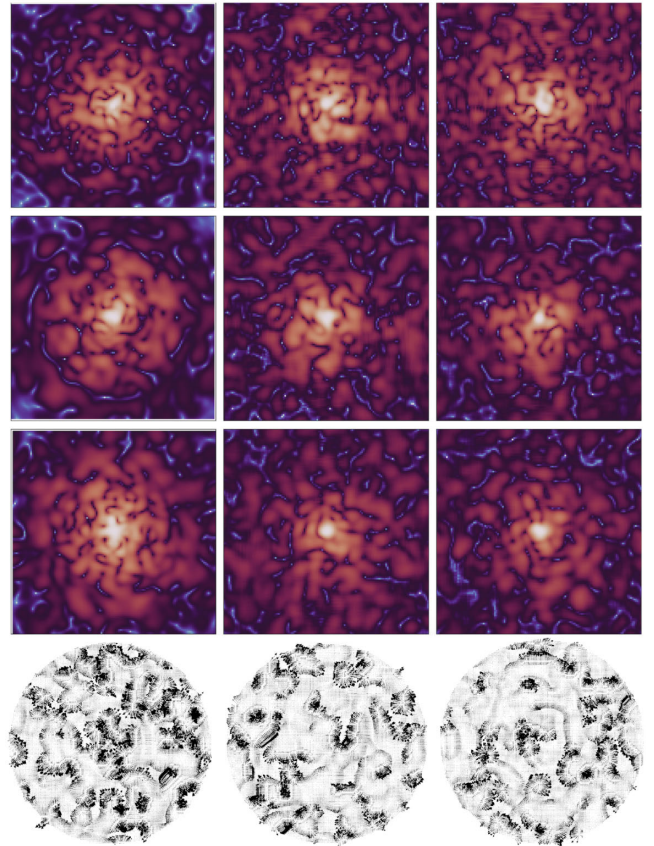

FIG. 1. Target, fitted, and average density profiles using the GA. The first, second, and third rows correspond to the galaxies ESO4880049, UGC11616, and F730V1, respectively. The vertical red line indicates the radius r_0 used in the weighted exponential function for the target density. The first column corresponds to the core-NFW profile, and the second column corresponds to the core-PISO profile. The continuous blue line represents the target density, while the orange dotted line illustrates the fitted density obtained in the 1000th generation. Finally, the green dotted line represents the average in time of the spatial averaged density of snapshots during 7 Gyr of evolution that we describe below; notice the that the evolution clearly distorts the density profile.

FIG. 2. The first, second, and third rows show snapshots of the density in the plane $z = 0$, for galaxies ESO4880049, UGC11616, and F730V1, respectively, assuming the core-NFW target profile. The first column corresponds to initial time, while the second and third columns correspond to times $t = 1$ and 2 Gyr, respectively. The fourth row shows snapshots at 0, 1 and 2 Gyr of the velocity field for the galaxy F730V1, for illustration.

guarantee the persistence of a core surrounded by an envelope, as well as the constancy of mass and total energy.

As initial conditions, we inject the wave function (8) at time $t = 0$, $\Psi(0, \vec{x}) = \Psi_0$ centered in the 3D cubic box $D = [-r_0, r_0]^3$. It is worth noticing that when the coefficients are fixed, the wave function can possess an overall momentum different from zero, calculated as $\vec{p}_0 = -i\hbar \sum_{j,k} a_k^* a_j \int_D \psi_k^* \nabla \psi_j d^3 x$. Then, we correct the initial wave function to be $\Psi(0, \vec{x}) = \Psi_0 e^{-i\vec{p}_0 \cdot \vec{x}/M}$, where $M := \int_D \rho d^3 x$ represents the total mass in the domain. This choice ensures that the initial wave function has zero total linear momentum, and the evolution remains with the core nearly at the center of the domain. The domain was discretized with a spatial resolution of $\Delta = r_0/128$ along the three spatial directions. To capture the temporal dynamics, a time resolution satisfying $\Delta t/\Delta < 0.25$ in code units was employed, and the evolution was carried out over a time-window of 2 Gyrs.
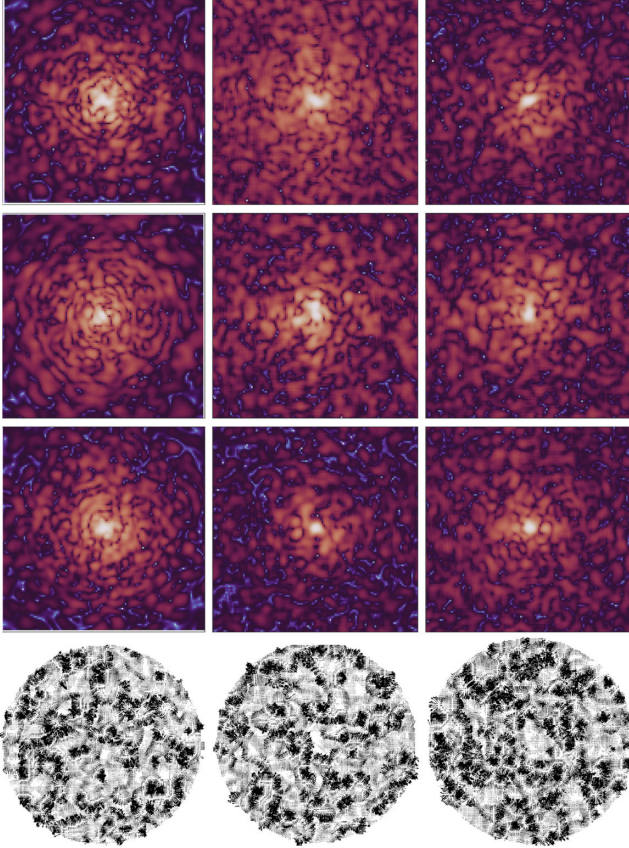
The evolution of each galaxy is depicted through snapshots of the density and velocity vector field in the $z = 0$ plane at times $t = 0$, 1, and 2 Gyr in Figs. 2 and 3. These simulations use the initial conditions with core-NFW and core-PISO target density profiles, respectively.

It is evident that even though the configurations are initially near a virialized state, they evolve and in fact the configurations do not remain stationary and not even in average, instead they develop some dynamics. In order to understand better the evolution of the whole configuration, we look into the time dependence of the core mass for each of the galaxies of the sample. The core mass M_c is the integral of the density (21) from the origin until r_c and its value as function of time is shown in Fig. 4 for six of the configurations during 7 Gyr. Notice that the core mass oscillates with an overall growing trend that can be understood as the accretion of matter from the granular envelope, indicating that the growth mass is due to collisional effects [47,48], interpreted as condensation in the kinetic regime [49] or wave condensation [50]. This slow, but never ending core mass growth, has been shown to happen after the saturation time [51]. This core mass
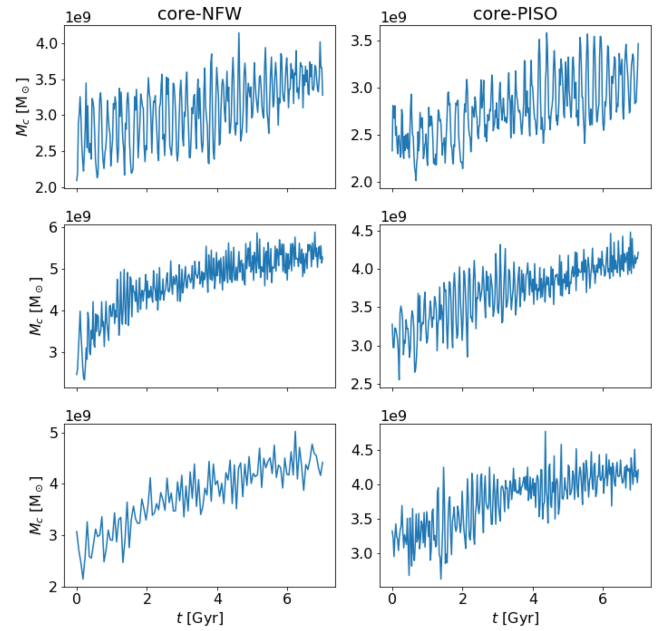

FIG. 3. The first, second, and third rows show snapshots of the density in the plane $z = 0$, corresponding to the galaxies ESO4880049, UGC11616, and F730V1, respectively, assuming the core-PISO target profile. The first column corresponds to initial time, while the second and third columns correspond to times $t = 1$ and 2 Gyr, respectively. The fourth row shows snapshots at 0, 1 and 2 Gyr of the velocity field for the galaxy F730V1, for illustration.

FIG. 4. Evolution of M_c as function of time during 7 Gyr. The first, second, and third rows correspond to the galaxies ESO4880049, UGC11616, and F730V1, respectively. The first column corresponds to the core-NFW profile, and the second column corresponds to the core-PISO profile. The plots indicate that the core accretes mass in the long term, which implies a time-dependent concentration of matter. This process is interpreted as the accretion from the granular envelope. This mass growth has been shown to happen after core saturation after relaxation [51] and seems to be universal in core-halo structures that evolve [49].
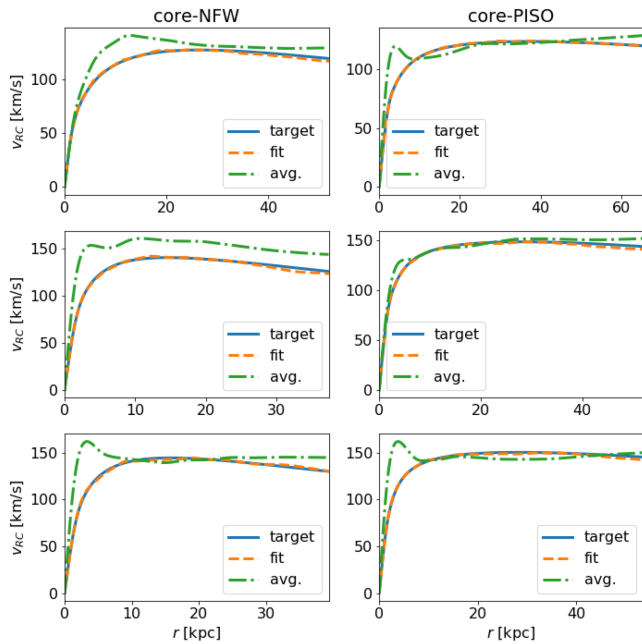
FIG. 5. Target, fitted, and average rotation curve of three galaxies of the sample. The first, second, and third rows correspond to ESO4880049, UGC11616, and F730V1, respectively. The first column corresponds to the core-NFW profile, and the second column corresponds to the core-PISO profile. The continuous blue line represents the rotation curve associated with the target density, while the orange dotted line illustrates the fitted density obtained in the 1000th generation. The green dotted line represents the time-average of the spatial averages during 7 Gyr of evolution.

growth seems inevitable and the reason why possibly any configuration with granular structure will lead to evolution and core growth. As a result, the dynamics is influenced and the average density in the evolution deviates from the averages of the initial data, an effect also described in [16].

The implication is that the redistribution of density will also distort the rotation curve. We illustrate this difference by calculating the spatiotemporal density average $\langle \rho \rangle$, which is now only a function of the radial coordinate. Once the average density is obtained, we compute the radial rotation curve as $v_{\rm RC} = \sqrt{Gm(r)/r}$, where $m(r)$ is the mass density integrated until radius r. For each halo, the results are presented in Fig. 5. The discrepancy between the initial and the evolved configuration is noticeable. The concentration of matter in the core region definitely changes the RC with a characteristic peak of a concentrated mass.

IV. CONCLUSIONS

We present a method to construct FDM halos, with multimode expansions characterized by a core-halo profile associated to observational rotation curves. The target

density profiles were of type core plus an envelope with NFW and pseudoisothermal profiles that fit rotation curves of a sample of LSB galaxies. While the core is dominated by the first term in an expansion in spherical harmonics, the envelope contains the expected granular structure. When averaged on the solid angle, the density profile approaches the target density that fits rotation curves.

Even though the constructed configurations are nearly virialized, it seems unavoidable the evolution of the configuration that degrades the quality of the RCs fittings. We then evolved these configurations during 7 Gyr and measured the core mass as function of time, we found the generic result, namely, the core permanently accretes matter from the granular envelope, an effect already measured after the formation and saturation time of cores [51], with a slow but permanent growth that goes as $t^{1/8}$. The core-halos are stable in the "collisionless" regime but they evolve due to "collisions" (granularities) on a secular timescale. Note that this is not an instability but a natural secular dynamical evolution, accompanied by a condensation process and the growth of the soliton. This is in agreement with kinetic theory as described in [47,48].

A direct implication of the core growth is that matter concentrates near the center of the galaxy and the rotation curve develops a characteristic peak at a small radius, observed in some galaxies (e.g., in [36]). A lesson from our analysis is that no matters how well RCs are fitted with a core surrounded a granular envelope, and how virialized to model is, FDM configurations will evolve and get distorted by the core accretion.

A considerable enhancement to this analysis would be the contribution of luminous matter during the evolution, which if gravitationally coupled to FDM and would influence the dynamics of the whole structure.

APPENDIX: CONNECTION BETWEEN THE WAVE DESCRIPTION AND THE KINETIC DESCRIPTION

In this Appendix, we discuss the connection between the wave description and the kinetic description. We recall the relation between the wave superposition coefficients $|\tilde{a}_{nl}|^2$ and the particle distribution function $f(\epsilon)$ following [16]. We then use this relation to recover the classical energy functionals and the classical virial theorem from the quantum ones in the WKB (high energy) limit.

1. Classical kinetic description based on the Vlasov-Poisson equations

In a classical description (applying for example to stellar systems or to the time-averaged envelope of DM halos) the density is given by

$$\rho = \int f d\mathbf{v}, \tag{A1}$$

where $f(\mathbf{r}, \mathbf{v}, t)$ is the distribution function for particles of mass m_B, i.e., $f(\mathbf{r}, \mathbf{v}, t)$ gives the mass density of particles with position $\mathbf{r}$ and velocity $\mathbf{v}$ at time t. It is normalized such that $\int f d\mathbf{r} d\mathbf{v} = M_{\text{envelope}}$. We assume that the envelope is spherically symmetric with a DF $f = f(\epsilon)$ that is a function of the energy alone. Such a DF determines a steady (virialized) state of the classical Vlasov-Poisson equations. We have introduced the energy per unit mass $\epsilon = E/m_B = v^2/2 + V$, where V is the gravitational potential. Eq. (A1) can then be rewritten as

$$\rho = \int_{V(r)}^{0} f(\epsilon) 4\pi \sqrt{2(\epsilon - V)} d\epsilon. \tag{A2}$$

In practice it is difficult to predict the DF f of the envelope resulting from the process of violent relaxation. Note that there is no rigorous derivation of the NFW and Burkert profiles so these profiles remain essentially empirical. Actually, a prediction of the DF may be attempted from the statistical theory of Lynden-Bell [52,53] However, this "naive" prediction leads to a DF with an infinite mass so it is necessary to take into account the evaporation of high energy particles to have a more physical model. This leads to the fermionic King model [54] where the "fermionic" nature of the DF arises from the specificities of the Vlasov equation in the Lynden-Bell statistical theory. In many cases "degeneracy" effects can be neglected leaving us with the classical King model. The King model determines a sequence of equilibrium states (indexed by the central concentration) ranging from a pure polytrope of index $n = 5/2$ to an isothermal distribution ($n = \infty$) [55,56]. It is shown that the King model at the critical point of marginal stability, just before the system undergoes the gravothermal catastrophe, gives a good agreement with the Burkert profile (see the comparison between the different density profiles reported in Fig. 18 of [56] and Fig. 1 of [57]. Therefore, the (fermionic) King model may be a relevant model of DM halos that is physically motivated.

2. Quantum wave description based on the Schrödinger-Poisson equations in the WKB approximation

The quantum wave description of DM halos is discussed in the main text. Because of the process of violent relaxation or gravitational cooling, the envelope of DM halos may be viewed as a superposition of excited states with energies E_{nl} and amplitude $\tilde{a}_{nl}$. This is similar to the orbits of particles with energies ϵ and DF $f(\epsilon)$ in classical systems. By contrast, the core (soliton) of quantum DM halos corresponds to the ground state of the Schrödinger-Poisson equations that has no counterpart in classical systems. Here, we focus on the envelope and we consider sufficiently high energies E so that the WKB approximation can be employed (see [16] for details).

In the WKB approximation (large E limit), the radial function is given by

$$R_{nl}(r) = \frac{N_{nl}}{r\sqrt{p(r)}} \sin\left[\frac{1}{\hbar} \int_{r_1}^{r} p(r') dr' + \frac{\pi}{4}\right], \tag{A3}$$

where

$$p(r) = \sqrt{2m_B \left(E_{nl} - \frac{l(l+1)\hbar^2}{2mr^2} - m_B V\right)} \tag{A4}$$

is the classical radial momentum. The normalization condition is chosen such that $\int_{r_1}^{r_2} R_{nl}(r)^2 r^2 dr = 1$ giving

$$N_{nl}^2 = \frac{1}{\int_{r_1}^{r_2} \frac{dr}{2p(r)}}, \tag{A5}$$

where we have approximated the square of the sine as $1/2$. In the above expressions, r_1 and r_2 are the turning points where p vanishes. The energy eigenvalues E_{nl} satisfy the Bohr-Sommerfeld quantization condition

$$\int_{r_1}^{r_2} p(r) dr = \pi\hbar\left(n + \frac{1}{2}\right). \tag{A6}$$

To compute the time-average density of the envelope we approximate the sum over n and l in Eq. (10) by integrals and write

$$\rho(r) = \frac{1}{4\pi} \int d\epsilon dl \frac{dn}{d\epsilon} R_{nl}(r)^2 (2l+1)|\tilde{a}_{nl}|^2 \tag{A7}$$

with $\epsilon = E_{nl}/m_B$. The Jacobian dn/dl can be obtained by differentiating the quantization condition from Eq. (A6) yielding

$$\frac{dn}{d\epsilon} = \frac{m^2}{\pi\hbar} \int_{r_1}^{r} \frac{dr}{p(r)}. \tag{A8}$$

Using this expression together with the WKB approximation for $R_{nl}(r)$ in Eqs. (A3) and (A5), a nice cancellation of terms occurs, leaving us with

$$\rho(r) = \frac{m_B^2}{4\pi^2\hbar} \int d\epsilon dl (2l+1)|\tilde{a}_{nl}|^2 \frac{1}{r^2 p(r)}. \tag{A9}$$

For a given ϵ and r, l ranges from 0 to $l_{\max}$ such that $\epsilon - l(l+1)\hbar^2/(2m_B^2 r^2) - V = 0$. If we assume that $|\tilde{a}_{nl}|^2$ depends only on $\epsilon = E_{nl}/m_B$ (in agreement with the corresponding assumption that $f = f(\epsilon)$ in the classical description) the integral over l can be easily performed with the change of variables $x = l(l+1)$ yielding

$$\rho(r) = \frac{m_B^3}{2\pi^2 \hbar^3} \int d\epsilon |\tilde{a}_{nl}|^2 \sqrt{2(\epsilon - V)}. \quad \text{(A10)}$$

Comparing Eqs. (A2) and (A10) the following relation is obtained [16]:

$$f(\epsilon) = \frac{m_B^3}{(2\pi\hbar)^3} |\tilde{a}_{nl}|^2. \quad \text{(A11)}$$

This equality is approximate in the sense that it is valid in the WKB limit. It is expected to hold only for eigenmodes with a high enough energy ϵ, i.e., for eigenmodes that describe the envelope of the DM halo. The soliton has to be treated independently as being the ground state of the SP equations. The interface between the soliton and the halo (with intermediate energies) may not be accurately described by the WKB approximation.

In conclusion, for a spherically symmetric halo with a particle distribution function $f(\epsilon)$, the density profile is given by Eq. (A2) and the wave is given by Eq. (10) with $|\tilde{a}_{nl}|^2$ given by Eq. (A11) in the WKB limit, i.e., for large energies. Using this kind of construction [15] have shown that the time-average envelope of FDM halos obtained in numerical simulations is well-fitted by the fermionic King model [54] giving further support to the claim made in [56] that the (fermionic) King model may be a good model of the envelope of DM halos.

3. WKB for functionals

Using the WKB approximation for $R_{nl}(r)$ [see Eqs. (A3) and (A5)], and proceeding as above, we find that the energy functional defined by Eq. (17) reduces to

$$E = \frac{2m_B^3}{\pi\hbar^3} \int d\epsilon |\tilde{a}_{nl}|^2 \sqrt{2(\epsilon - V)} \epsilon r^2 dr. \quad \text{(A12)}$$

Using the identity from Eq. (A11) it can be rewritten as

$$E = 16\pi^2 \int d\epsilon f(\epsilon) \epsilon \sqrt{2(\epsilon - V)} r^2 dr \quad \text{(A13)}$$

or as

$$E = \int f(\epsilon)\epsilon d\mathbf{r} d\mathbf{v}. \quad \text{(A14)}$$

Recalling that $\epsilon = v^2/2 + V$ we obtain

$$E = \int f \frac{v^2}{2} d\mathbf{r} d\mathbf{v} + 2W. \quad \text{(A15)}$$

Finally, recalling the identity $E = K + 2W$ established in Sec. II A and using Eq. (A15), we find that the quantum kinetic energy coincides, in the high energy limit, with the classical kinetic energy

$$K = \int f \frac{v^2}{2} d\mathbf{r} d\mathbf{v}. \quad \text{(A16)}$$

This agreement is expected, but not trivial, since K in Eq. (12) is expressed in terms of the wave function $\psi(\mathbf{r}, t)$—a function of position only—while K in Eq. (A16) is expressed in terms of the DF $f(\mathbf{r}, \mathbf{v}, t)$—a function of position and velocity (reducing to a function of the energy ϵ for spherically symmetric systems).

Finally, we emphasize that the total energy (the one which is conserved) is $E_{\text{tot}} = K + W$. It differs from the energy E (related to the eigenenergies) which is given by $E = K + 2W$. The factor 2 arises because the system is self-gravitating (instead of being subjected to an external potential).

[1] Abril Suárez, Victor H. Robles, and Tonatiuh Matos, A review on the scalar field/Bose-Einstein condensate dark matter model, Astrophys. Space Sci. Proc. **38,** 107 (2014).

[2] Lam Hui, Wave dark matter, Annu. Rev. Astron. Astrophys. **59,** 247 (2021).

[3] Elisa G. M. Ferreira, Ultra-light dark matter, Astron. Astrophys. Rev. **29,** 7 (2021).

[4] Pierre-Henri Chavanis, Self-gravitating Bose-Einstein condensates, in *Quantum Aspects of Black Holes*, edited by Xavier Calmet (Springer International Publishing, Cham, 2015), pp. 151–194.

[5] Jens C. Niemeyer, Small-scale structure of fuzzy and axion-like dark matter, Prog. Part. Nucl. Phys. **113,** 103787 (2020).

[6] Hsi-Yu Schive, Tzihong Chiueh, and Tom Broadhurst, Cosmic structure as the quantum interference of a coherent dark wave, Nat. Phys. **10,** 496 (2014).

[7] Philip Mocz, Mark Vogelsberger, Victor H. Robles, Jesús Zavala, Michael Boylan-Kolchin, Anastasia Fialkov, and Lars Hernquist, Galaxy formation with BECDM I. Turbulence and relaxation of idealized haloes, Mon. Not. R. Astron. Soc. **471,** 4559 (2017).

[8] Jan Veltmaat, Jens C. Niemeyer, and Bodo Schwabe, Formation and structure of ultralight bosonic dark matter halos, Phys. Rev. D **98**, 043509 (2018).

[9] Philip Mocz, Anastasia Fialkov, Mark Vogelsberger, Fernando Becerra, Mustafa A. Amin, Sownak Bose, Michael Boylan-Kolchin, Pierre-Henri Chavanis, Lars Hernquist, Lachlan Lancaster, Federico Marinacci, Victor H. Robles, and Jesús Zavala, First star-forming structures in fuzzy cosmic filaments, Phys. Rev. Lett. **123**, 141301 (2019).

[10] Simon May and Volker Springel, Structure formation in large-volume cosmological simulations of fuzzy dark matter: Impact of the non-linear dynamics, Mon. Not. R. Astron. Soc. **506**, 2603 (2021).

[11] Bodo Schwabe and Jens C. Niemeyer, Deep zoom-in simulation of a fuzzy dark matter galactic halo, Phys. Rev. Lett. **128**, 181301 (2022).

[12] Hsi-Yu Schive, Ming-Hsuan Liao, Tak-Pong Woo, Shing-Kwong Wong, Tzihong Chiueh, Tom Broadhurst, and W. Y. Pauchy Hwang, Understanding the core-halo relation of quantum wave dark matter from 3D simulations, Phys. Rev. Lett. **113**, 261302 (2014).

[13] Bodo Schwabe, Jens C. Niemeyer, and Jan F. Engels, Simulations of solitonic core mergers in ultralight axion dark matter cosmologies, Phys. Rev. D **94**, 043513 (2016).

[14] Julio F. Navarro, Carlos S. Frenk, and Simon D. M. White, A universal density profile from hierarchical clustering, Astrophys. J. **490**, 493 (1997).

[15] Shan-Chang Lin, Hsi-Yu Schive, Shing-Kwong Wong, and Tzihong Chiueh, Self-consistent construction of virialized wave dark matter halos, Phys. Rev. D **97**, 103523 (2018).

[16] Tomer D. Yavetz, Xinyu Li, and Lam Hui, Construction of wave dark matter halos: Numerical algorithm and analytical constraints, Phys. Rev. D **105**, 023512 (2022).

[17] Mateja Gosenca, Andrew Eberhardt, Yourong Wang, Benedikt Eggemeier, Emily Kendall, J. Luna Zagorac, and Richard Easther, Multifield ultralight dark matter, Phys. Rev. D **107**, 083014 (2023).

[18] H.-Y. Schive, T. Chiueh, T. Broadhurst, and K.-W. Huang, Contrasting galaxy formation from quantum wave dark matter, ψDM, with ΛCDM, using Planck and Hubble data, Astrophys. J. **818**, 89 (2016).

[19] V. Iršič, M. Viel, M. G. Haehnelt, J. S. Bolton, and G. D. Becker, First constraints on fuzzy dark matter from Lyman-α forest data and hydrodynamical simulations, Phys. Rev. Lett. **119**, 031302 (2017).

[20] E. Armengaud, N. Palanque-Delabrouille, C. Yèche, D. J. E. Marsh, and J. Baur, Constraining the mass of light bosonic dark matter using SDSS Lyman-α forest, Mon. Not. R. Astron. Soc. **471**, 4606 (2017).

[21] Renée Hlozek, Daniel Grin, David J. E. Marsh, and Pedro G. Ferreira, A search for ultralight axions using precision cosmological data, Phys. Rev. D **91**, 103512 (2015).

[22] Brandon Bozek, David J. E. Marsh, Joseph Silk, and Rosemary F. G. Wyse, Galaxy UV-luminosity function and reionization constraints on axion dark matter, Mon. Not. R. Astron. Soc. **450**, 209 (2015).

[23] Abir Sarkar, Rajesh Mondal, Subinoy Das, Shiv. K. Sethi, Somnath Bharadwaj, and David J. E. Marsh, The effects of the small-scale DM power on the cosmological neutral hydrogen (HI) distribution at high redshifts, J. Cosmol. Astropart. Phys. 04 (2016) 012.

[24] Tanja Rindler-Daller and Paul R. Shapiro, Angular momentum and vortex formation in Bose-Einstein-condensed cold dark matter haloes, Mon. Not. R. Astron. Soc. **422**, 135 (2012).

[25] Victor H. Robles and T. Matos, Exact solution to finite temperature SFDM: Natural cores without feedback, Astrophys. J. **763**, 19 (2013).

[26] B. Li, T. Rindler-Daller, and P. R. Shapiro, Cosmological constraints on Bose-Einstein-condensed scalar field dark matter, Phys. Rev. D **89**, 083536 (2014).

[27] Abril Suárez and Pierre-Henri Chavanis, Cosmological evolution of a complex scalar field with repulsive or attractive self-interaction, Phys. Rev. D **95**, 063515 (2017).

[28] Abril Suárez and Pierre-Henri Chavanis, Jeans type instability of a complex self-interacting scalar field in general relativity, Phys. Rev. D **98**, 083529 (2018).

[29] Vincent Desjacques, Alex Kehagias, and Antonio Riotto, Impact of ultralight axion self-interactions on the large scale structure of the Universe, Phys. Rev. D **97**, 023529 (2018).

[30] J. A. R. Cembranos, A. L. Maroto, S. J. Núñez Jareño, and H. Villarrubia-Rojo, Constraints on anharmonic corrections of Fuzzy Dark Matter, J. High Energy Phys. 08 (2018) 073.

[31] L. Arturo Ureña López, Scalar field dark matter with a cosh potential, revisited, J. Cosmol. Astropart. Phys. 06 (2019) 009.

[32] Pierre-Henri Chavanis, Jeans mass-radius relation of self-gravitating Bose-Einstein condensates and typical parameters of the dark matter particle, Phys. Rev. D **103**, 123551 (2021).

[33] Vicente Delgado and Antonio Muñoz Mateo, Self-interacting superfluid dark matter droplets, Mon. Not. R. Astron. Soc. **518**, 4064 (2022).

[34] F. S. Guzmán and L. Arturo Ureña López, Evolution of the Schrödinger-Newton system for a self-gravitating scalar field, Phys. Rev. D **69**, 124033 (2004).

[35] David J. E. Marsh and Ana-Roxana Pop, Axion dark matter, solitons and the cusp-core problem, Mon. Not. R. Astron. Soc. **451**, 2479 (2015).

[36] Tula Bernal, Lizbeth M. Fernández-Hernández, Tonatiuh Matos, and Mario A. Rodríguez-Meza, Rotation curves of high-resolution LSB and SPARC galaxies with fuzzy and multistate (ultralight boson) scalar field dark matter, Mon. Not. R. Astron. Soc. **475**, 1447 (2018).

[37] W. J. G. de Blok, S. S. McGaugh, and V. C. Rubin, High-resolution rotation curves of low surface brightness galaxies. II. Mass models, Astron. J. **122**, 2396 (2001).

[38] S. S. McGaugh, V. C. Rubin, and W. J. G. de Blok, High-resolution rotation curves of low surface brightness galaxies. I. Data, Astron. J. **122**, 2381 (2001).

[39] John Kormendy and K. C. Freeman, Scaling laws for dark matter halos in late-type and dwarf spheroidal galaxies, IAU Symp. **220**, 377 (2004).

[40] M. Spano, M. Marcelin, P. Amram, C. Carignan, B. Epinat, and O. Hernandez, GHASP: An H-alpha kinematic survey of spiral and irregular galaxies—V. Dark matter distribution in 36 nearby spiral galaxies, Mon. Not. R. Astron. Soc. **383**, 297 (2007).

[41] F. Donato, G. Gentile, P. Salucci, C. Frigerio Martins, M. I. Wilkinson, G. Gilmore, E. K. Grebel, A. Koch, and R. Wyse, A constant dark matter halo surface density in galaxies, Mon. Not. R. Astron. Soc. **397,** 1169 (2009).

[42] Pierre-Henri Chavanis, Predictive model of bec dark matter halos with a solitonic core and an isothermal atmosphere, Phys. Rev. D **100,** 083022 (2019).

[43] Iván Álvarez-Rios and Francisco S Guzmán, Exploration of simple scenarios involving fuzzy dark matter cores and gas at local scales, Mon. Not. R. Astron. Soc. **518,** 3838 (2022).

[44] Iván Álvarez-Rios, Francisco S. Guzmán, and Paul R. Shapiro, Effect of boundary conditions on structure formation in fuzzy dark matter, Phys. Rev. D **107,** 123524 (2023).

[45] F. S. Guzmán and L. Arturo Ureña López, Gravitational cooling of self-gravitating Bose condensates, Astrophys. J. **645,** 814 (2006).

[46] Argelia Bernal and F. S. Guzmán, Scalar field dark matter: Nonspherical collapse and late-time behavior, Phys. Rev. D **74,** 063504 (2006).

[47] Ben Bar-Or, Jean-Baptiste Fouvry, and Scott Tremaine, Relaxation in a fuzzy dark matter halo, Astrophys. J. **871,** 28 (2019).

[48] Pierre-Henri Chavanis, Landau equation for self-gravitating classical and quantum particles: Application to dark matter, Eur. Phys. J. Plus **136,** 703 (2021).

[49] D. G. Levkov, A. G. Panin, and I. I. Tkachev, Gravitational Bose-Einstein condensation in the kinetic regime, Phys. Rev. Lett. **121,** 151301 (2018).

[50] Benedikt Eggemeier and Jens C. Niemeyer, Formation and mass growth of axion stars in axion miniclusters, Phys. Rev. D **100,** 063528 (2019).

[51] Jiajun Chen, Xiaolong Du, Erik W. Lentz, David J. E. Marsh, and Jens C. Niemeyer, New insights into the formation and growth of boson stars in dark matter halos, Phys. Rev. D **104,** 083022 (2021).

[52] D. Lynden-Bell, Statistical mechanics of violent relaxation in stellar systems, Mon. Not. R. Astron. Soc. **136,** 101 (1967).

[53] P. H. Chavanis, J. Sommeria, and R. Robert, Statistical mechanics of two-dimensional vortices and collisionless stellar systems, Astrophys. J. **471,** 385 (1996).

[54] Pierre-Henri Chavanis, On the coarse-grained evolution of collisionless stellar systems, Mon. Not. R. Astron. Soc. **300,** 981 (1998).

[55] Ivan R. King, The structure of star clusters. II. Steady-state velocity distributions, Astron. J. **70,** 376 (1965).

[56] Pierre-Henri Chavanis, Mohammed Lemou, and Florian Mehats, Models of dark matter halos based on statistical mechanics: The classical king model, Phys. Rev. D **91,** 063531 (2015).

[57] Pierre-Henri Chavanis, Predictive model of fermionic dark matter halos with a quantum core and an isothermal atmosphere, Phys. Rev. D **106,** 043538 (2022).